Advanced Functional Materials

ADVANCED FUNCTIONAL MATERIALS
www.afm-journal.de

RESEARCH ARTICLE OPEN ACCESS

Two-Photon Grayscale Lithography (2GL) of High Mechanical and Optical Quality 3D Silica Glass Microstructures

Jonathan L. G. Schneider[1] | Jiajie Liang[2] | Paul Somers[2] | Martin Wegener[1,2] | Jens Bauer[2,3]

[1]Institute of Applied Physics (APH), Karlsruhe Institute of Technology (KIT), Karlsruhe, Germany | [2]Institute of Nanotechnology (INT), Karlsruhe Institute of Technology (KIT), Karlsruhe, Germany | [3]Institute of Applied Materials (IAM), Karlsruhe Institute of Technology (KIT), Karlsruhe, Germany

Correspondence: Martin Wegener (martin.wegener@kit.edu) | Jens Bauer (jens.bauer@kit.edu)

Received: 25 December 2025 | **Revised:** 18 June 2026 | **Accepted:** 8 July 2026

Keywords: 2GL | 3D microstructures | diffractive optical element | low mechanical damping | micro-mechanical testing | POSS | silica glass | two-photon grayscale lithography | two-photon polymerization

ABSTRACT

Two-photon grayscale lithography (2GL) is the latest evolution in two-photon polymerization laser 3D printing, combining unmatched surface quality and throughput by continuous laser power modulation that dynamically controls the print feature size (voxel) to smoothly blend contours despite coarse slicing. To reconstruct shapes, 2GL solves an inverse problem requiring parametrization of the voxel size and their underlying print parameters, which is specific to a given feedstock resist and so far, only available for a few commercial polymers. This paper establishes a 2GL 3D-printing route for the rapid manufacturing of complex silica glass micro- and nanostructures of unprecedented quality and accuracy, substantially advancing glass micro-fabrication. This is enabled by a pre-glass polyhedral oligomeric silsesquioxane (POSS) resist, engineered for high polymerization sensitivity and dynamic range. Together with a routine to identify optimal grayscale parameters for such custom resists, we realize the use of the 2GL process at maximal print speed while maintaining high loading of the silicon-oxygen POSS-cluster source. Mechanical resonators with quality factors $> 1\,000$, optical components with < 3 nm roughness and nanoscale diffractive patterns are demonstrated, opening new pathways in photonics, precision mechanics, and metamaterials. The introduced grayscale parameter identification routine provides a framework for extending 2GL-printing to a broader material range.

1 | Introduction

Two-photon polymerization (2PP) 3D-printing of micro- and nanostructures has become a routine and commercially available manufacturing technology [1–4]. Herein, a laser focus is scanned with respect to a photosensitive material (resist), and the laser power is switched on and off as desired to locally polymerize the resist. After exposure, the unpolymerized material is removed by development in a solvent (developer). In this manner, a large range of organic architectures have been realized by researchers around the globe with applications in optics [3, 5, 6], biology [7–9], mechanics [10–12], and micro-robotics [13–15]. Lately, emerging routes based on specialized resists enable the manufacturing of a growing number of inorganic materials along the same lines as well [16–23]. Hybrid organic–inorganic resists incorporate metal or metalloid elements into monomers with photocurable organic ligands. After printing, the resulting hybrid preforms are converted into inorganic structures via thermal treatments.

Jonathan L. G. Schneider and Jiajie Liang contributed equally to this work

Resist design based on polyhedral oligomeric silsesquioxane (POSS) chemistry provides a facile platform to manufacture silica glass structures [23]. POSS molecules, with the general formula ($SiO_{1.5}$), are composed of cage-like silicon-oxygen cores to which a large variety of functional groups can attach. Acrylate functionalization enables the 2PP-printing of 3D pre-glass templates, which a simple baking step in air atmosphere above 650°C converts to dense SiO_2 glass. In this way, glass fabrication of microscopic 3D structures such as metamaterials or compound lens systems [24], unrealizable by techniques such as conventional top-down etching and 2.5D imprinting [25, 26], is now possible.

Two-photon grayscale lithography (2GL) [27] is a conceptual refinement of 2PP 3D printing, which simultaneously enables faster printing and improved quality with respect to standard 2PP 3D printing by not only switching the laser on/off while scanning the laser focus but rather modulating the laser power continuously between zero and some maximum value. With higher laser power, the exposed material volume (voxel) at a given laser position increases, allowing rapid printing of interior volumes, e.g., of optical microlenses. Conversely, lower laser powers decrease the voxel size. Hence, coordinated modulation of the voxel size continuously blends contours along surfaces, reducing or even eliminating staircasing ripples that otherwise arise from layer-by-layer printing. As a result, unmatched surface quality with nanometer roughness is achieved, alongside high throughput, using coarse slicing with layer spacings of 1 µm and above. However, such grayscale laser printing requires solving an inverse problem: To reconstruct a targeted 3D micro- or nanostructure, one needs to identify the necessary laser power at each focus position. The solution is presently only available via proprietary software or brute force methods. In essence, the algorithm to solve the inverse problem needs information as to how the volume and shape of the voxel exposed at one laser-focus position depends on the laser power. This information can be cast into the form of phenomenological parameters – which depend on the resist system used and have only been demonstrated for proprietary polymeric resists so far [28–32].

Herein, we identify these phenomenological parameters for a customized hybrid organic–inorganic POSS-resist system, demonstrating a 2GL 3D-printing route for the facile manufacturing of 3D silica glass micro- and nanostructures of unprecedented quality. With respect to our previous work [23], the POSS-resist is modified with a high-sensitivity photoinitiator. Based on identified optimum 2GL parameters, we fabricate a variety of complex 3D silica-glass microstructures of high fidelity and demonstrate excellent mechanical and optical quality. We measure mechanical quality factors well exceeding 1 000, which is about two orders of magnitude larger than for corresponding polymers [33], and report Young's moduli of 71 GPa, closely matching pristine fused silica. We present microlenses with optical-grade surface finish with a root mean square (RMS) roughness below 3 nm and showcase optical performance with complex holographic diffractive optical elements (DOEs). Finally, we provide a general routine for identifying the phenomenological parameters required to solve the inverse problem within 2GL, establishing a framework that enables systematic parameter discovery for future inorganic and organic resist systems.

2 | Two-Photon Grayscale Lithography (2GL) of POSS-Glass Resists

Successful 2GL requires a resist design that is tailored to the printer hardware to access a sufficient bandwidth of adjustable voxel sizes, as well as the identification of a phenomenological parametrization which correctly maps the input print parameters to the voxel size. This parametrization generally depends on the objective-lens point-spread function (PSF) and consequently, is specific to each resist-objective-lens combination. Herin, 2GL 3D-printing was performed using a Quantum X lithography system (Nanoscribe GmbH & Co. KG) with two different objective lenses, the so-called "medium-feature set" (25×/NA0.8 LCI Plan-Neofluar, Zeiss) and the "small-feature set" (63×/NA1.4 Plan-Apochromat Oil DIC, Zeiss). The Quantum X platform implements the inverse-design parametrization that underlies the 2GL approach, which maps the laser power to the voxel shape and size, via the proprietary software nanoPrintX (v.4.17.3). This parametrization generally depends on the objective-lens point-spread function and the resist's cross-linking behavior, with the resist dynamic range, defined by the ratio of the damage and polymerization thresholds, setting the usable print parameter window and the accessible bandwidth of adjustable voxel sizes. Consequently, the 2GL parametrization is specific to each resist-objective-lens combination. Successful 2GL requires a resist design with a dynamic range that is tailored to the printer hardware, as well as identification of a parametrization that correctly establishes the phenomenological correlation between voxel geometry and the print parameters.

2.1 | Resist Formulation

To best exploit 2GL, a resist requires two key characteristics: (i) a high sensitivity, enabling it to reliably polymerize at low exposure dose, allowing maximal print speeds at coarse slicing; and (ii) a high dynamic range, which is the printing window between the polymerization and the damage exposure dose thresholds, respectively, in order to maximize the range of adjustable voxel sizes accessible to the 2GL process. Both characteristics strongly depend on the choice and the concentration ratios of the resist's photoinitiator-monomer-combination [1, 34]. In the context of hybrid resists for fabricating inorganics via thermolysis, the optimization of such is further subject to the additional constraint to maximize the target inorganic constituent loading.

We herein engineered a modified formulation of our previously introduced pre-glass resist system based on POSS chemistry [23], which is initiated with the highly efficient Norrish type II photoinitiator, BDBuABnCHx (BBK) [34], demonstrating substantially increased sensitivity and dynamic range up to the 2GL setup's maximum speed while maintaining a high POSS-cluster loading (Figure S1, S2 and Table S1). Our modified formulation contains 90 wt.% of an acrylate-functionalized POSS monomer as the cross-linkable silicon-oxygen nanocluster source, 9.5 wt.% of a copolymerizing trifunctional acrylic monomer, and 0.5 wt.% of the BBK photoinitiator. Measurements of single voxel-lines printed across a range of laser power and scan speed combinations demonstrated that our resist possesses extensive dynamic range (Figure S2a–d). The resist achieves a multiphoton polymerization sensitivity figure of merit (FOM) [34] as high as 81.7, marking an increase of more than an order of magnitude over our previous formulation with the Norrish type I photoinitiator Irgacure 369, and well exceeding the commercial resists IP-Dip, IP-S, and IP-L (Nanoscribe GmbH & Co. KG) (Figure S2e).

2.2 | 2GL Parameter Optimization Routine

To establish the 2GL parametrization of custom-made resist systems, such as the POSS-glass resist, we introduce a systematic routine based on iterative test prints of selected benchmark structures that enables the coordinated identification of the underlying conventional 2PP parameters and dependent 2GL-specific parameters (Figure 1). We choose structures that challenge the 2GL process in order to critically assess a given parameterization. We utilize plano-convex microlenses as volumetric objects, whose slight curvature perpendicular to the build direction makes them highly sensitive to staircasing artifacts [3, 35, 36]; chiral metamaterial unit cells with complex 3D layouts [37], which evaluate the quality of curved features and sharp edges in all spatial directions; and simple cuboids to rapidly assess general shape accuracy and dynamic range. Following the visualized workflow, the routine optimizes parameters based on the indicated quality criteria as observed via in situ imaging, scanning-electron microscopy (SEM) and/or confocal microscopy. Beginning by setting a focus "scan speed" (at the "Start" in the figure), the routine works through four sets of print tests, sweeping through combinations of the indicated parameters. The initial "Dose Sweep" rapidly identifies the meaningful limits of the conventional 2PP parameter space, which the subsequent "2PP Sweep" refines to combinations enabling well-resolved structures, which however exhibit significant staircasing. The following "2GL Sweep" then adjusts the grayscale parameters controlling the dynamic voxel size modulation to identify a combination of 2PP and 2GL parameters which removes the staircasing and related artifacts for the coarsest possible slicing, and hence highest throughput. To achieve maximal shape accuracy, the final "Voxel Compensation" identifies a correction factor which compensates for the vertically elongated ellipsoidal voxel shape by compressing vertical design features. A detailed step-by-step description of the workflow and evaluated parameter sets for the POSS-glass resist are provided in the Supporting Information (Section S2.5. 2GL Parameter Optimization Routine, Table S7–S11).

By applying the routine to the POSS-glass resist, we achieved both rapid printing speed and high structure quality at the same time. Figure 1 compares metamaterial (Figure 1b) and microlens (Figure 1c) benchmark structures, each fabricated using either the small-feature set via 2GL or conventional 2PP. For both structures, we demonstrate 2GL prints with a slicing as coarse as 0.6 µm, which maintains smooth surfaces and sharply resolved edges. For identical hatching and slicing parameters, and hence the same print times, the conventional 2PP prints are subject to severe staircasing. Reduced slicing to improve the quality of the 2PP prints comes at the cost of increased print time. For the metamaterial test structure, print quality on par with 2GL at 0.6 µm slicing required a reduction of the 2PP slicing down to 0.05 µm. For the volumetric microlenses, the same approach could not achieve microlenses with surface qualities fully matching the 2GL counterparts for any setting, as refined slicing to alleviate the staircasing caused the emergence of localized surface artifacts [36]. Comparing best-quality structures, the ratio of the print times of the 2GL and the 2PP structures with 0.6 and 0.05 µm slicing, respectively, demonstrates that our 2GL POSS-glass route realizes an up to sevenfold throughput improvement over the corresponding conventional 2PP (Tables S4, S5). To probe that our 2GL routine translates across different resists, we have applied the routine to our previous POSS resist formulation [23] whose Norrish type I initiation mechanism significantly differs from our current formulation, successfully demonstrating 2GL with the medium-feature set (Section S2.5. 2GL Parameter Optimization Routine, Figures S5–S7 and Tables S3, S6).

3 | Experimental Results

3.1 | 3D Silica Glass Microstructures

By applying the introduced 2GL routine (Figure 1) to the modified POSS resist, we fabricated complex 3D silica glass microstructures of unprecedented structural quality, with smooth surfaces, free from staircasing artifacts, and with excellent shape accuracy down to sharply resolved smallest details. Figure 2 depicts representative structures, printed with the 2GL small-feature set and thermolyzed to glass at 700°C in air (Figure S3), which critically assess the capability of the 2GL glass fabrication route across diverse and challenging geometries. This selection includes the Benchy boat (Figure 2a,e) [38], a widely used 3D-printing benchmark spanning a range of feature sizes and shapes within a single object; a triply periodic minimal surface (TPMS) shell, as a mathematically continuous 3D membrane structure (Figure 2b,f) [39]; a Buckyball, which comprises large overhangs of thin strut elements with various orientations (Figure 2c,g); and a Fresnel lens as a volumetric optic with both smooth surfaces and sharp edges (Figure 2d,h). All structures are printed in excellent quality, with noteworthy details including well-resolved small features, such as the Benchy boat's steering wheel inside the cabin and the chimney on top (Figure 2a,e); the smooth 3D curvature of the thin TPMS surface (Figure 2f); the near-ideally straight Buckyball rods (Figure 2g) and the sharp Fresnel lens edges (Figure 2h). A feature size down to 1 µm is obtainable for complex 3D structures with the utilized optical setup and is demonstrated in Figure S10. Larger structures printed with the medium-feature set for both the original and modified POSS formulations are provided in Figures S8 and S9, respectively. Additional silica glass microlenses and chiral metamaterial unit cells are shown in Figure 4a and Figures S8–S10.

3.2 | Static Mechanical Experiments

Quasi-static in situ uniaxial compression tests with cylindrical micropillars (Figure S11) demonstrated that our POSS glass exhibits well-reproducible excellent mechanical properties. Figure 3a,b shows a SEM image of a representative silica glass micropillar prior to loading, alongside the corresponding measured stress-strain curve. In the experiments, the specimen strain was quantified within a gauge section between two markers, which were tracked via digital-image cross-correlation (DIC). A total of 12 micropillars with SEM-measured diameters of 14.90 ± 0.09 µm and two different height-to-diameter aspect ratios of 2.4 and 2.8 were characterized via two compression

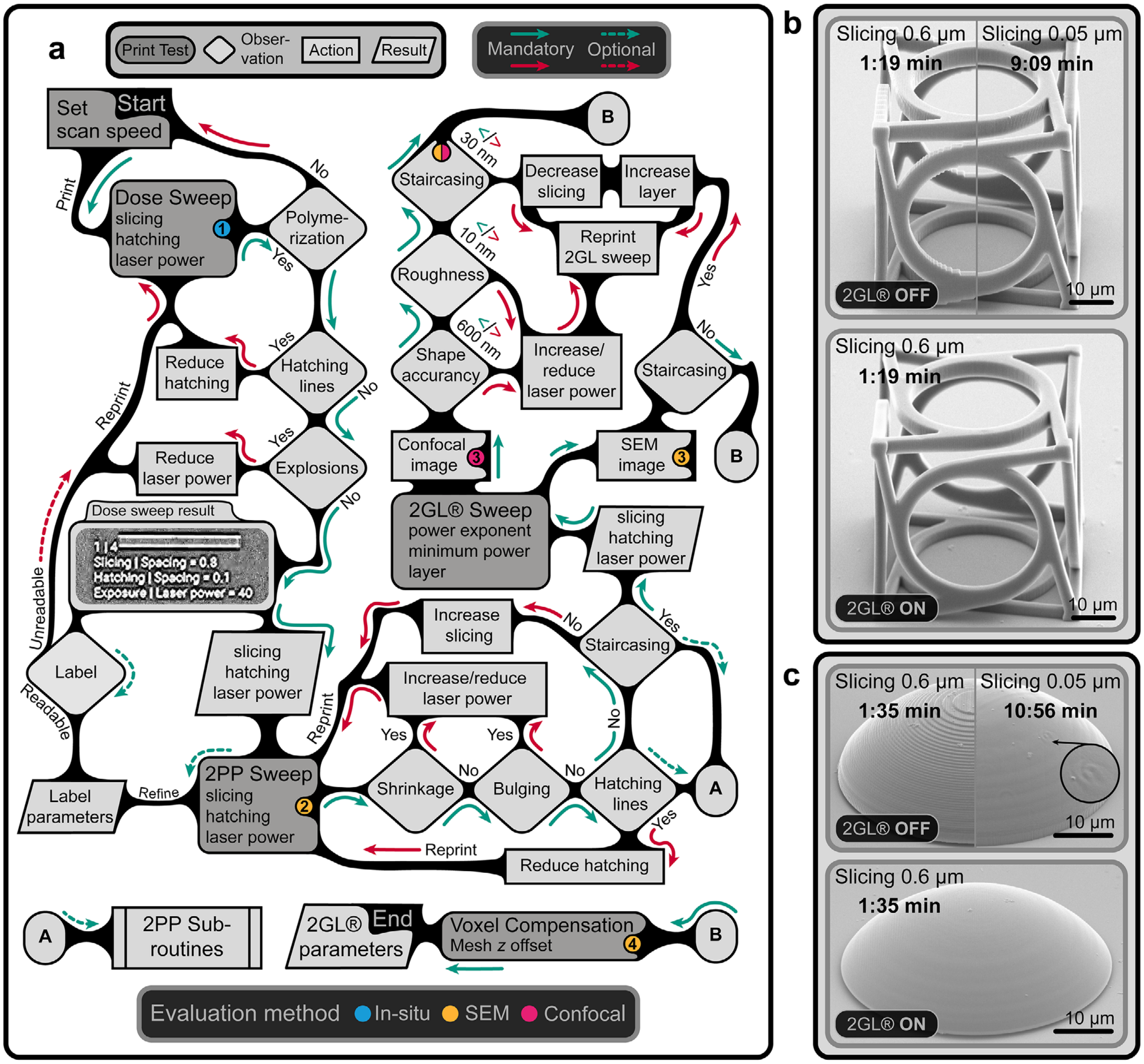

FIGURE 1 | (a) General routine to determine 2GL printing parameters for custom resists via a series of four print tests. Green arrows indicate the main route, red arrows denote reiterations. Dashed lines are optional tasks. Each print test systematically varies the listed parameters while all others remain fixed. For structure evaluation, in situ imaging on the printer, SEM, and/or confocal microscopy are conducted. The image inset illustrates a result of the 'Dose Sweep'. Polymeric 3D chiral metamaterial microstructures (b) and microlenses (c) printed with the evaluated 2PP and 2GL parameters from the POSS-based resist with BBK utilizing the small-feature set. For each structure, the used slicing and print time are indicated and compared for prints with fine/coarse slicing (2GL OFF) and 2GL (2GL ON). The circular inset on the microlens demonstrates remaining surface artifacts, even at fine slicing, while the 2GL-printed lens exhibits a smooth surface.

loading cycles with a constant applied strain rate of 0.2% s^{-1} (Movie S1). The first predominantly linear-elastic loading cycle up to ~2% strain served to extract Young's modulus (E), found as 70.99 ± 3.95 GPa. This measurement closely matches the reported values for high-quality commercial fused silica glass [40, 41], which we attribute to the herein achieved high structural fidelity free from undesired artifacts. The second loading cycle until failure displayed elastic-plastic-type behavior with substantial deformability up to a maximum strain (ε_{max}) of 22.5 ± 4.0% and 16.4 ± 6.9% for aspect ratios of 2.4 and 2.8, respectively, as well as ultra-high strength until brittle fracture. Our in situ image data (Movie S1) suggest the observed extended deformation behavior may largely stem from post-yield buckling while the intrinsic material behavior remains predominantly brittle. In good agreement with our data, elastic Euler column buckling for a pillar with an aspect ratio (AR) of 2.4 is expected at an applied strain ($\varepsilon_{el} = \pi^2/(16k^2AR^2)$) of 11%, with the effective length factor ($k = 1$) matching the observed fixed-sliding boundary condition behavior [42]. Such extended buckling of silica glass requires resistance to extreme stresses, which is enabled by harnessing substantial material-strengthening size effects, where the population and size of preexisting flaws is limited by the finite extrinsic size

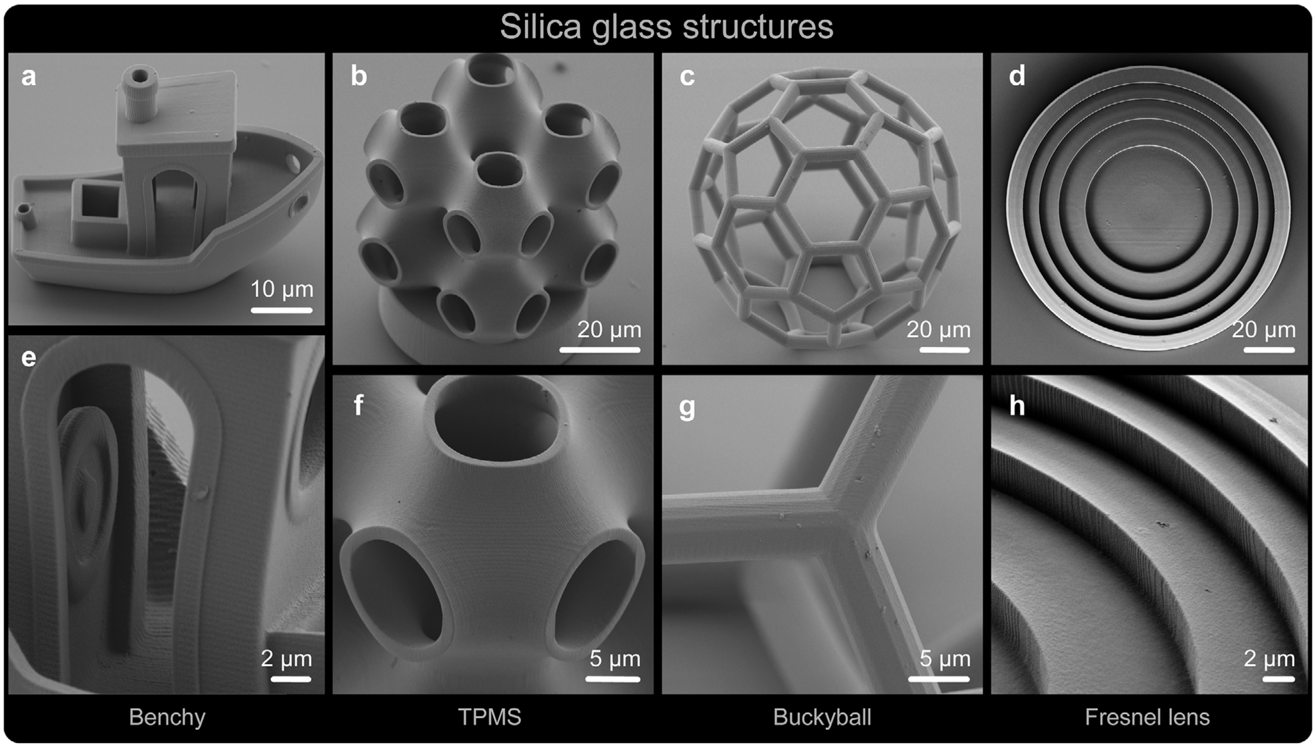

FIGURE 2 | SEM images gallery of high-quality POSS-glass microstructures made by means of the introduced 2GL printing routine and tailored POSS resist formulation. (a–d) Top and oblique views of a Benchy boat, a triply periodic minimal surface (TPMS) shell, a Buckyball and a Fresnel lens. (e–h) Close-up views demonstrating excellent surface quality and shape accuracy down to the smallest details. All structures were 2GL-printed with the small-feature set and thermally converted to silica glass at 700°C in air.

[43]. Additional contributions to the observed behaviors may be attributed to a certain extent of plastic shear flow [44–46], as reported in similar micropillar experiments. The effect is widely understood based on bond-switching events whose activation becomes increasingly favorable as the surface-to-volume ratio rises, and which can be strongly enhanced by electron irradiation [46]. Contributions from pressure-induced densification effects and anisotropic structure have been discussed as well [45, 47]. We measured yield strengths (σ_y) of 1.82 ± 0.24 GPa and compressive strengths (σ_{max}) of 5.46 ± 0.28 GPa, both in good agreement with our previously reported values [23] and comparable to other reported silica micropillars [44]. Notably, while our σ_{max} under buckling influence can be considered a conservative measurement, it is ~1.5 GPa higher than previously.

3.3 | Dynamic Mechanical Experiments and Quality Factors (Q)

To determine the mechanical quality factor (Q) – a measure of a structure's damping behavior, where high Q indicates low damping and energy loss, and vice versa – we adopted a dynamic resonance measurement approach using piezo-excited micro-tuning-forks [33]. Tuning forks with a tip-to-tip distance of a = 200 μm were 2GL-printed from our hybrid POSS resist, as well as from the commercial polymer 2GL resists IP-S and IP-DIP2 (Table S12). During the glass conversion, the silica forks isotropically contracted (Figure S4 and Table S2), yielding a final distance of a = 125 μm. Figure 3c,d shows that the glass forks exhibit excellent structure quality, on par with the IP-S counterparts printed with the manufacturer 2GL-parameters. All samples were printed with baseplates for mounting them into our previously described home-built laser-scanning confocal microscope with integrated laser-Doppler vibrometry [48, 49]. In the measurements, the tuning forks were excited time-harmonically via a piezoelectric actuator in ambient atmosphere. Amplitudes of the tips and vertical excitation amplitudes at the fork base were measured and extracted by DIC, while out-of-plane displacements were collected by vibrometry. The tip amplitudes were normalized to the excitation amplitudes of the fork handle.

Figure 3e–h shows the measured amplitudes and phase lags around the resonance of the fundamental vibration modes (Movie S2) of the forks from the POSS resist, both in the as-printed state and the final glass, along with comparison specimens from the commercial IP-S and IP-DIP2. Q values were obtained by a least-squares Lorentzian fit of the squared amplitudes. For IP-S and IP-DIP2, we found Q = 21.97 ± 0.40 and Q = 28.75 ± 0.50, respectively. With respect to the commercial IP resists, the as-printed POSS had lower values of Q = 11.60 ± 0.23. However, after the glass conversion, these values increased to Q = 1479.95 ± 7.53 along with a more than 100-fold higher amplitude, exceeding the commercial polymers by two orders of magnitude, as expected for silica glass. Experiments in vacuum, which eliminate the air friction, can be expected to further increase Q by another order of magnitude [33]. These high Q values correspond to very low losses, which our 2GL glass fabrication route makes accessible within high-precision free-form microstructures for research fields that require low mechanical damping, such as topological phononic systems and

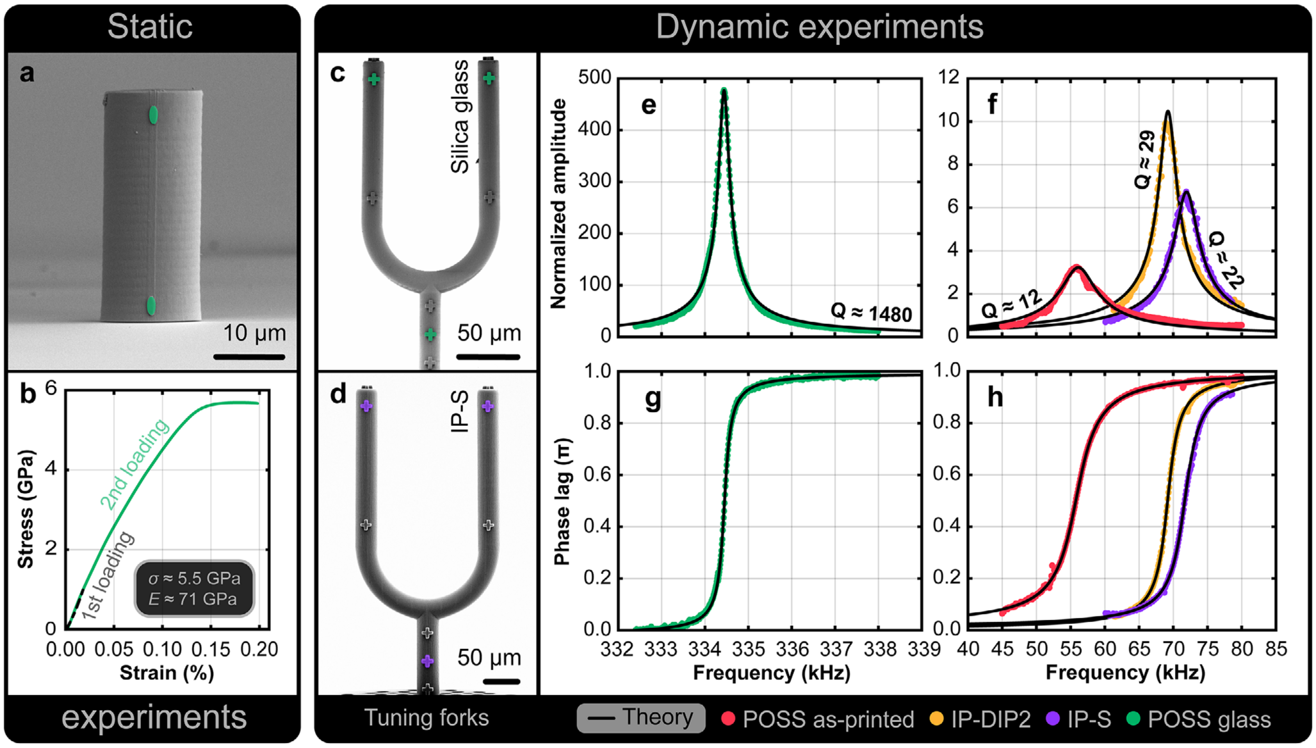

FIGURE 3 | Static and dynamic mechanical properties of the POSS-glass. (a) SEM image of a representative silica-glass micropillar for quasi-static compression, markers for digital image correlation (DIC) strain measurement are highlighted in green. (b) Corresponding stress-strain curve comprised of two loading cycles, measuring Young's modulus and strength, respectively. (c–d) SEM images of a POSS-glass micro-tuning-fork for dynamic resonance measurements and comparison specimens from the commercial polymer IP-S, markers for DIC analysis are highlighted in color. (e–f) Measured resonance curves and derived quality factors (Q) extracted by least-squares Lorentzian fits overlayed as black lines. (g–h) Corresponding phase lags of the fundamental vibration mode for each resonance curve.

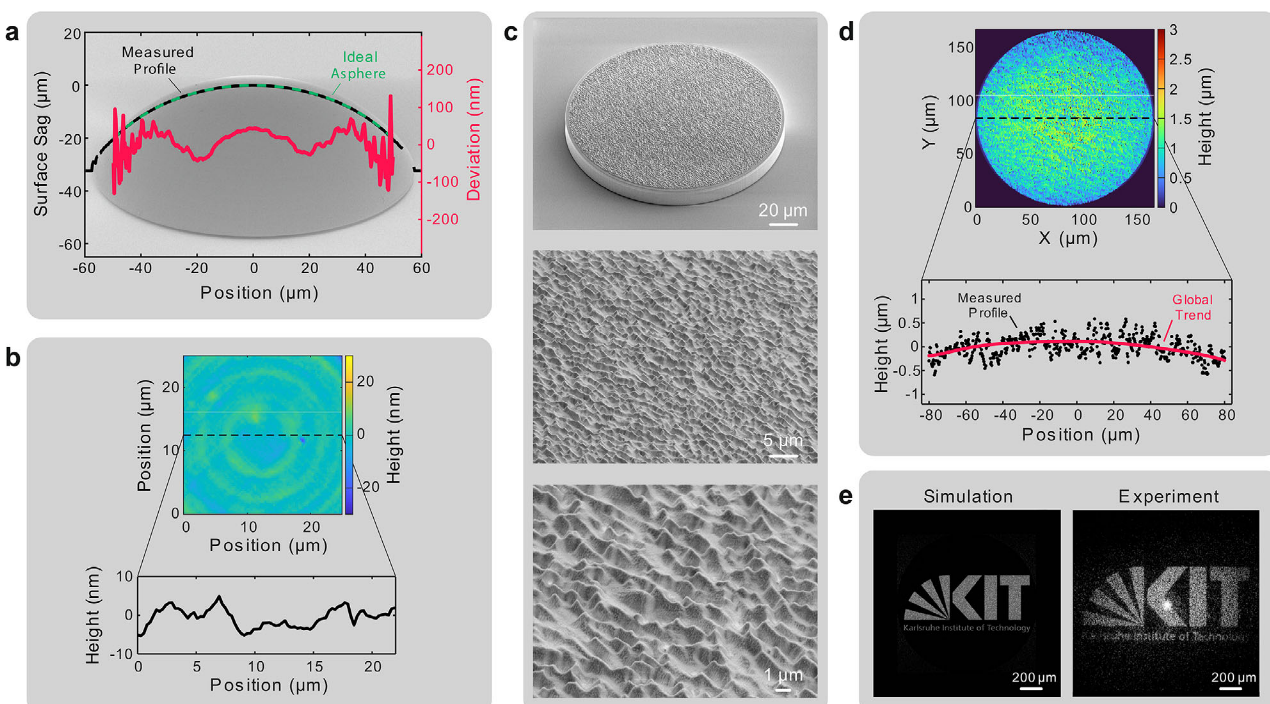

FIGURE 4 | Optical quality of the 2GL POSS-glass. (a) SEM image and optical profilometry section of a microlens; (b) surface roughness map of the microlens center area and extracted profile; (c) SEM images of a diffractive optical element (DOE) designed to create a holographic projection of a KIT logo; (d) optical profilometry data of the DOE, along with a 2D height profile through the DOE center; (e) simulated and experimentally obtained holographic images.

mechanical metamaterials. Measurements for the POSS resist formulation with Irgacure 369 as the photoinitiator and details about conducting the experiments are provided in the Sections S3, S4 (Figures S12 and S13).

3.4 | Optical Experiments

Surface profilometry measurements demonstrate that our 2GL POSS-glass achieves an optically smooth finish up to the most challenging print geometries (Figure 4a). As a benchmark, we manufactured aspherical microlenses printed with their optical axis oriented perpendicular to the build direction, where the slightly curved center area is notorious for staircasing artifacts [3, 35]. Our lenses, with a base diameter of 114 µm and a sagittal (sag) height of 32 µm, exhibited a peak-to-valley deviation of ± 130 nm with respect to an ideal asphere. From the $25 \times 25\ \mu m^2$-size center area, we measured a root mean square (RMS) roughness of 2.4 nm (Figure 4b), corresponding to an RMS-to-sag ratio of merely 0.0075%, which outperforms our previously reported results [23] by a factor of more than six. Optics fabricated with this below $\sim \lambda/100$ roughness, where λ refers to visible wavelengths, will have very low surface-scattering induced losses and aberrations which would otherwise contribute to a reduced-quality point spread function (PSF) of an optical system. High-quality PSFs are critical for high resolution imaging in visible light applications [50, 51]. The surface quality of our optics is competitive with that of commercial silica microlenses produced by reactive ion etching or ion-exchange processes [52] and rivals state-of-the-art 2GL-printed polymer lenses, for which RMS roughnesses of 4–17 nm were reported, and peak-to-valley deviations without iterative correction were within 70 nm–1.2 µm [29, 32].

Showcasing optical performance with complex micro-parts, we present a 160 µm-size holographic diffractive optical element (DOE) comprised of a 3D nanostructured continuous-relief pattern (Figure 4c). The DOE pattern manipulates the wavefront of light traveling through the structure to create a holographic projection of our target design, the Karlsruhe Institute of Technology (KIT) logo, via concerted constructive and destructive interference. Fabrication of the DOE pattern atop a flat base support enabled controlled geometric contraction during glass conversion while preserving the free-form relief. The general contraction behavior of the material system is characterized in Figure S4. This sidesteps the challenges of controlling anisotropic contractions of such thin structures, an approach that enables large-area patterns but imposes design constraints [53]. Optical profilometry confirmed that our 2GL POSS-glass routine achieved near-ideal uniformity, with the DOE pattern atop a flat base support being free from undesired process-induced deformations (Figure 4d). A polynomial fit of the measured height map confirmed global flatness within ± 198 nm across the entire pattern. The height variation of the DOE pattern was within ± 600 nm, only slightly less than the designed height profile of ± 690 nm. The optical performance is experimentally verified (Figures S14), with the acquired holographic images showing good agreement with the ideal simulation predictions (Figure 4e). The experimental images are well resolved with legible small text features and little distortion and noise, demonstrating the projection quality of our glass DOE on par with reported 2PP printed polymeric DOEs [5]. Beyond optical performance, silica glass micro-optics also offer improved thermal stability and higher laser damage thresholds, which are advantageous for high-power applications [54]. The visible brighter zero-order spot in the center originates from undiffracted light, a characteristic feature of diffraction optics that can be circumvented through off-axis projection designs [5]. The presented overall quality demonstrates our 2GL POSS-glass route as viable for the rapid manufacturing of compact and robust glass micro-optics featuring complex 3D nanopatterns, which may hardly be achieved via conventional top-down etching techniques.

4 | Conclusion

Multiphoton 3D laser printing of 3D micro- and nanostructures composed of organic materials, such as polymers and hydrogels, has already enabled numerous applications. However, other applications may require temperature stability at high temperatures, chemical inertness, or purely elastic rather than viscoelastic behavior, i.e., large mechanical quality factors. In this regard, the printing of inorganic materials has recently been steadily advancing, with silica glass being a prominent important example.

Here, we have established a route for the grayscale multiphoton 3D laser printing of silica glass using a POSS-based resist with focus scan velocities as high as 250 $mm \cdot s^{-1}$, which substantially advances glass manufacturing beyond conventional multiphoton printing approaches. This advance was enabled by the development of a tailored resist composition compatible with the commercial 2GL process, and an optimization routine to identify suitable grayscale parameters of the proprietary technique for such a custom resist. As a result, we have demonstrated complex glass microstructures with unprecedented surface finish and shape accuracy, including high-quality optical components, such as microlenses with < 3 nm RMS roughness and diffractive optical elements comprised of nanoscale patterns, as well as mechanical micro-tuning-fork resonators with quality factors beyond 1 000 – values that have previously only been achieved with significantly more involved manufacturing processes [33]. The ability to print complex, low-loss 3D glass architectures with high throughput opens new opportunities in optics and photonics, precision mechanics, and emerging classes of micro- and nano-metamaterials. Users from other groups may simply apply the herein presented resist and print parameters to manufacture parts with the same ease and efficiency previously available only for a limited set of commercial polymer resists.

Finally, this work presents the first demonstration of 2GL-printing using a custom hybrid organic–inorganic resist, establishing a routine for identifying resist-specific print parameters. We anticipate it to provide a practical tool for extending high-quality 2GL printing to a yet broader range of materials.

Author Contributions

Jonathan L. G. Schneider: data curation, formal analysis, investigation, visualization, writing – original draft, writing – review & editing, methodology, validation, software. **Jiajie Liang:** data curation, formal analysis, investigation, writing – original draft, writing – review &

editing, visualization, methodology, validation, software. **Paul Somers:** investigation, Writing – review and editing, formal analysis, validation, software. **Martin Wegener**: writing – review & editing, project administration, resources, funding acquisition, conceptualization, supervision, validation, methodology. **Jens Bauer**: conceptualization, project administration, resources, writing – review & editing, funding acquisition, supervision, validation, methodology.

Acknowledgements

We acknowledge funding by the Deutsche Forschungsgemeinschaft (DFG, German Research Foundation) under Germany's Excellence Strategy for the Excellence Cluster "3D Matter Made to Order" (2082/1–390761711; 2082/2–390761711) as well as under the grant BA 5778/2-1, by the Carl Zeiss Foundation, by the Helmholtz program Materials Systems Engineering and by the Karlsruhe Nano Micro Facility (KNMFi). The authors thank Florian Feist (KIT) for the synthesis of the BBK photoinitiator.

Open access funding enabled and organized by Projekt DEAL.

Funding

DFG 2082/1–390761711; DFG 2082/2–390761711; DFG BA 5778/2-1; Karlsruhe Nano Micro Facility (KNMFi)

Conflicts of Interest

The authors declare no conflicts of interest.

Data Availability Statement

All data related to this work is published in the open-access data repository of the Karlsruhe Institute of Technology (KIT) [https://doi.org/10.35097/r4fthp8jhpfaj5zg].

References

1. T. Baldacchini, *Three-Dimensional Microfabrication Using Two-Photon Polymerization* (William Andrew, an imprint of Elsevier, 2020).

2. P. Somers, A. Münchinger, S. Maruo, C. Moser, X. Xu, and M. Wegener, "The Physics of 3D Printing With Light," *Nature Reviews Physics* 6 (2023): 99–113, https://doi.org/10.1038/s42254-023-00671-3.

3. H. Wang, W. Zhang, D. Ladika, et al., "Two-Photon Polymerization Lithography for Optics and Photonics: Fundamentals, Materials, Technologies, and Applications," *Advanced Functional Materials* 33 (2023): 2214211, https://doi.org/10.1002/adfm.202214211.

4. E. Skliutas, G. Merkininkaite, S. Maruo, et al., "Multiphoton 3D Lithography," *Nature Reviews Methods Primers* 5 (2025): 15, https://doi.org/10.1038/s43586-025-00386-y.

5. H. Wang, Y. Liu, Q. Ruan, et al., "Off-Axis Holography With Uniform Illumination via 3D Printed Diffractive Optical Elements," *Advanced Optical Materials* 7 (2019): 1900068, https://doi.org/10.1002/adom.201900068.

6. M. D. Schmid, A. Toulouse, S. Thiele, S. Mangold, A. M. Herkommer, and H. Giessen, "3D Direct Laser Writing of Highly Absorptive Photoresist for Miniature Optical Apertures," *Advanced Functional Materials* 33 (2023): 2211159, https://doi.org/10.1002/adfm.202211159.

7. N. Munding, M. Fladung, Y. Chen, et al., "Bio-Metamaterials for Mechano-Regulation of Mesenchymal Stem Cells," *Advanced Functional Materials* 34 (2024): 2301133, https://doi.org/10.1002/adfm.202301133.

8. F. Colombo, M. Taale, F. Taheri, et al., "Two-Photon Laser Printing to Mechanically Stimulate Multicellular Systems in 3D," *Advanced Functional Materials* 34 (2024): 2303601, https://doi.org/10.1002/adfm.202303601.

9. M. Wostry, A. Berkes, P. Kiefer, M. Wegener, and R. Scherließ, "Aerodynamic Performance of Tailored Microparticles as Carriers in Dry Powder Inhaler Formulations Made by Multi-Focus Multi-Photon 3D Laser Printing," *Communications Materials* 6 (2025): 184, https://doi.org/10.1038/s43246-025-00913-0.

10. T. Tancogne-Dejean, M. Diamantopoulou, M. B. Gorji, C. Bonatti, and D. Mohr, "3D Plate-Lattices: An Emerging Class of Low-Density Metamaterial Exhibiting Optimal Isotropic Stiffness," *Advanced Materials* 30 (2018): 1803334, https://doi.org/10.1002/adma.201803334.

11. A. Jelinek, S. Zak, M. J. Cordill, D. Kiener, and M. Alfreider, "Nanoscale Printed Tunable Specimen Geometry Enables High-Throughput Miniaturized Fracture Testing," *Materials & Design* 234 (2023): 112329, https://doi.org/10.1016/j.matdes.2023.112329.

12. Y. Chen, J. L. G. Schneider, K. Wang, et al., "Anomalous Frozen Evanescent Phonons," *Nature Communications* 15 (2024): 8882, https://doi.org/10.1038/s41467-024-52956-5.

13. G. Adam, A. Benouhiba, K. Rabenorosoa, C. Clévy, and D. J. Cappelleri, "4D Printing: Enabling Technology for Microrobotics Applications," *Advanced Intelligent Systems* 3 (2021): 2000216, https://doi.org/10.1002/aisy.202000216.

14. Q. Ji, J. Moughames, X. Chen, et al., "4D Thermomechanical Metamaterials for Soft Microrobotics," *Communications Materials* 2 (2021): 93, https://doi.org/10.1038/s43246-021-00189-0.

15. M. Salah, Y. Bordes, C. Clévy, et al., "Towards Bi-Material 3D Printed Soft Microrobots using Two-Photon Polymerisation," *Journal of Micro and Bio Robotics* 21 (2025): 7, https://doi.org/10.1007/s12213-025-00185-4.

16. J. Bauer, A. Schroer, R. Schwaiger, and O. Kraft, "Approaching Theoretical Strength in Glassy Carbon Nanolattices," *Nature Materials* 15 (2016): 438–443, https://doi.org/10.1038/nmat4561.

17. A. Vyatskikh, S. Delalande, A. Kudo, X. Zhang, C. M. Portela, and J. R. Greer, "Additive Manufacturing of 3D Nano-Architected Metals," *Nature Communications* 9 (2018): 593, https://doi.org/10.1038/s41467-018-03071-9.

18. J. Bauer, C. Crook, A. Guell Izard, et al., "Additive Manufacturing of Ductile, Ultrastrong Polymer-Derived Nanoceramics," *Matter* 1 (2019): 1547–1556, https://doi.org/10.1016/j.matt.2019.09.009.

19. D. Gonzalez-Hernandez, S. Varapnickas, G. Merkininkaite, et al., "Laser 3D Printing of Inorganic Free-Form Micro-Optics," *Photonics* 8 (2021): 577, https://doi.org/10.3390/photonics8120577.

20. X. Wen, B. Zhang, W. Wang, et al., "3D-Printed Silica With Nanoscale Resolution," *Nature Materials* 20 (2021): 1506–1511, https://doi.org/10.1038/s41563-021-01111-2.

21. L. Yang, H. Hu, A. Scholz, et al., "Laser Printed Microelectronics," *Nature Communications* 14 (2023): 1103, https://doi.org/10.1038/s41467-023-36722-7.

22. F. Li, S.-F. Liu, W. Liu, et al., "3D Printing of Inorganic Nanomaterials by Photochemically Bonding Colloidal Nanocrystals," *Science* 381 (2023): 1468–1474, https://doi.org/10.1126/science.adg6681.

23. J. Bauer, C. Crook, and T. Baldacchini, "A Sinterless, Low-Temperature Route to 3D Print Nanoscale Optical-Grade Glass," *Science* 380 (2023): 960–966, https://doi.org/10.1126/science.abq3037.

24. Z. Hong, P. Ye, D. A. Loy, and R. Liang, "Integrated 3D Printing of Transparency-on-Demand Glass Microstructure," *Advanced Optical Materials* 13 (2025): 2500390, https://doi.org/10.1002/adom.202500390.

25. W. Menz, J. Mohr, and O. Paul, *Microsystem Technology* (Wiley, 2000), https://doi.org/10.1002/9783527613007.

26. L. J. Guo, "Nanoimprint Lithography: Methods and Material Requirements," *Advanced Materials* 19 (2007): 495–513, https://doi.org/10.1002/adma.200600882.

27. Nanoscribe GmbH & Co. KG. Introducing Two-Photon Grayscale Lithography accessed July 16 2026), https://www.nanoscribe.com/en/microfabrication-technologies/2gl-two-photon-grayscale-lithography/.

28. T. Aderneuer, O. Fernández, and R. Ferrini, "Two-Photon Grayscale Lithography for Free-Form Micro-Optical Arrays," *Optics Express* 29 (2021): 39511, https://doi.org/10.1364/OE.440251.

29. L. Siegle, S. Ristok, and H. Giessen, "Complex Aspherical Singlet and Doublet Microoptics by Grayscale 3D Printing," *Optics Express* 31 (2023): 4179, https://doi.org/10.1364/OE.480472.

30. J. Weinacker, S. Kalt, A. Huber, et al., "Multi-Photon 3D Laser Micro-Printed Plastic Scintillators for Applications in Low-Energy Particle Physics," *Advanced Functional Materials* 35 (2024): 2413215, https://doi.org/10.1002/adfm.202413215.

31. P. Kiefer, V. Hahn, S. Kalt, Q. Sun, Y. M. Eggeler, and M. Wegener, "A Multi-Photon (7 × 7)-Focus 3D Laser Printer based on a 3D-Printed Diffractive Optical Element and a 3D-Printed Multi-Lens Array," *Light: Advanced Manufacturing* 4 (2024): 3, https://doi.org/10.37188/lam.2024.003.

32. S. Wagner, L. Siegle, S. Haeusler, et al., "From Two-Photon Grayscale Lithography to Scalable Replication: Enabling Complex Aspherical Micro-Optics for Mass Production," *Advanced Optical Materials* 13 (2025): 02089, https://doi.org/10.1002/adom.202502089.

33. J. Köpfler, T. Frenzel, J. Schmalian, and M. Wegener, "Fused-Silica 3D Chiral Metamaterials via Helium-Assisted Microcasting Supporting Topologically Protected Twist Edge Resonances With High Mechanical Quality Factors," *Advanced Materials* 33 (2021): 2103205, https://doi.org/10.1002/adma.202103205.

34. P. Kiefer, V. Hahn, M. Nardi, et al., "Sensitive Photoresists for Rapid Multiphoton 3D Laser Micro- and Nanoprinting," *Advanced Optical Materials* 8 (2020): 2000895, https://doi.org/10.1002/adom.202000895.

35. X. Zhou, Y. Hou, and J. Lin, "A Review on the Processing Accuracy of Two-Photon Polymerization," *AIP Advances* 5 (2015): 030701, https://doi.org/10.1063/1.4916886.

36. A. Bertoncini, Y. Tanguy, and A. Tungal, "Advancement in two-photon grayscale lithography," in 3D Printed Optics and Additive Photonic Manufacturing III, Strasbourg, France (2022), https://doi.org/10.1117/12.2620974.

37. T. Frenzel, M. Kadic, and M. Wegener, "Three-Dimensional Mechanical Metamaterials with a Twist," *Science* 358 (2017): 1072–1074, https://doi.org/10.1126/science.aao4640.

38. #3DBenchy, The jolly 3D printing torture-test, accessed July 16, 2026, https://www.3dbenchy.com/.

39. O. Al-Ketan and R. K. Al-Rub, "Multifunctional Mechanical Metamaterials Based on Triply Periodic Minimal Surface Lattices," *Advanced Engineering Materials* 21 (2019): 1900524, https://doi.org/10.1002/adem.201900524.

40. S. Inaba, S. Fujino, and K. Morinaga, "Young's Modulus and Compositional Parameters of Oxide Glasses," *Journal of the American Ceramic Society* 82 (1999): 3501–3507, https://doi.org/10.1111/j.1151-2916.1999.tb02272.x.

41. R. N. Widmer, D. Bischof, J. Jurczyk, M. Michler, J. Schwiedrzik, and J. Michler, "Smooth or not: Robust fused silica micro-components by femtosecond-laser-assisted etching," *Materials & Design* 204 (2021): 109670, https://doi.org/10.1016/j.matdes.2021.109670.

42. S. P. Timoshenko and J. M. Gere, *Theory of Elastic Stability* (Dover publ, 2009).

43. G. Brambilla and D. N. Payne, "The Ultimate Strength of Glass Silica Nanowires," *Nano Letters* 9 (2009): 831–835, https://doi.org/10.1021/nl803581r.

44. R. Lacroix, G. Kermouche, J. Teisseire, and E. Barthel, "Plastic Deformation and Residual Stresses in Amorphous Silica Pillars Under Uniaxial Loading," *Acta Materialia* 60 (2012): 5555–5566, https://doi.org/10.1016/j.actamat.2012.07.016.

45. G. Kermouche, G. Guillonneau, J. Michler, J. Teisseire, and E. Barthel, "Perfectly Plastic Flow in Silica Glass," *Acta Materialia* 114 (2016): 146–153, https://doi.org/10.1016/j.actamat.2016.05.027.

46. S. Bruns, C. Minnert, L. Pethö, J. Michler, and K. Durst, "Room Temperature Viscous Flow of Amorphous Silica Induced by Electron Beam Irradiation," *Advanced Science* 10 (2023): 2205237, https://doi.org/10.1002/advs.202205237.

47. C. L. Rountree, D. Vandembroucq, M. Talamali, E. Bouchaud, and S. Roux, "Plasticity-Induced Structural Anisotropy of Silica Glass," *Physical Review Letters* 102 (2009): 195501, https://doi.org/10.1103/PhysRevLett.102.195501.

48. M. F. Groß, J. L. G. Schneider, Y. Wei, et al., "Tetramode Metamaterials as Phonon Polarizers," *Advanced Materials* 35 (2023): 2211801, https://doi.org/10.1002/adma.202211801.

49. M. F. Groß, J. L. G. Schneider, Y. Chen, M. Kadic, and M. Wegener, "Dispersion Engineering by Hybridizing the Back-Folded Soft Mode of Monomode Elastic Metamaterials With Stiff Acoustic Modes," *Advanced Materials* 36 (2024): 2307553, https://doi.org/10.1002/adma.202307553.

50. S. Thiele, K. Arzenbacher, T. Gissibl, H. Giessen, and A. M. Herkommer, "3D-Printed Eagle Eye: Compound Microlens System for Foveated Imaging," *Science Advances* 3 (2017): 1602655, https://doi.org/10.1126/sciadv.1602655.

51. L. Huang, Z. Huang, D. Liu, et al., "Full-Color Imaging With a 3D Nanoprinted Fiber Endoscope," *Optics Letters* 51 (2026): 37–40, https://doi.org/10.1364/OL.584435.

52. H. Ottevaere, R. Cox, H. P. Herzig, et al., "Comparing Glass and Plastic Refractive Microlenses Fabricated With Different Technologies," *Journal of Optics A: Pure and Applied Optics* 8 (2006): S407–S429, https://doi.org/10.1088/1464-4258/8/7/S18.

53. D. Zhu, J. Zhang, Q. Xu, and Y. Li, "Two-Photon Polymerization of Silica Glass Diffractive Micro-Optics With Minimal Lateral Shrinkage," *Optics Express* 31 (2023): 36037, https://doi.org/10.1364/OE.499528.

54. D. Gailevicius, R. Zvirblis, K. Galvanauskas, G. Bataviciute, and M. Malinauskas, "Calcination-Enhanced Laser-Induced Damage Threshold of 3D Micro-Optics Made With Laser Multi-Photon Lithography," *Photonics* 10 (2023): 597, https://doi.org/10.3390/photonics10050597.

Supporting Information

Additional supporting information can be found online in the Supporting Information section.

Supporting File 1: adfm77318-sup-0001-SuppMat.docx.

Supporting File 2: adfm77318-sup-0002-MovieS1.mp4.

Supporting File 3: adfm77318-sup-0003-MovieS2.mp4